Extreme Mechanics Letters 29 (2019) 100451

Contents lists available at ScienceDirect

Extreme Mechanics Letters

journal homepage: www.elsevier.com/locate/eml

Effects of material heterogeneity on self-rolling of strained membranes

Cheng Chen [a], Pengfei Song [b,c,d], Fanchao Meng [a], Pengfei Ou [a], Guoqiang Lan [a], Xinyu Liu [c], Jun Song [a,*]

[a] Department of Materials Engineering, McGill University, Montréal, Québec H3A0C5, Canada
[b] Department of Mechanical Engineering, McGill University, Montréal, Québec H3A0C3, Canada
[c] Department of Mechanical and Industrial Engineering, University of Toronto, Toronto, Ontario M5S3G8, Canada
[d] Department of Electrical and Electronic Engineering, Xi'an Jiaotong-Liverpool University, 111 Ren'ai Road, Suzhou, China

ARTICLE INFO

Article history:
Received 31 December 2018
Received in revised form 20 February 2019
Accepted 23 March 2019
Available online 27 March 2019

ABSTRACT

The present work studies the effects of strained membranes. An analytical framework has been established to predict self-rolling curvatures of strained bilayer membranes containing heterogeneous material elements. The accuracy of the framework is validated through molecular dynamics (MD) simulations on the heterogeneous $CdTe_xS_{1-x}$/CdTe bilayer system. Moreover, numerical simulations using finite-element modeling (FEM) have been performed to examine the role of heterogeneous elements in the complex helical rolling. It has been demonstrated that both the rolling direction and rollup curvature can be predictively controlled by modulating the material heterogeneity and layer thickness. The present study points to a new pathway towards predictive design and tuning of complex 3D structures based on strained membranes through incorporation of heterogeneous elements.

1. Introduction

The strain driven self-rolling of bi- and multi-layer strained membranes [1–8] enables programmable shape transformation, and subsequently controllable tuning of properties and functionalities [9–15], providing an attractive engineering strategy for diverse applications including elecromechanical/micro-electromechanical systems (NEMS/MEMS) [16], sensors [17,18], microrobotics [19,20], drug delivery [21,22], and optoelectronics [23–26] as well as artificial biomimetic structures [27–35].

A central aspect in self-rolling is the control of the driving force, namely the mechanical strain within the layered system. Recent technological developments of lithography-based procedures including photolithography [36], scanning lithography [37], soft lithography [38], and nanocontact printing [39] enable the incorporation of more complex compositional and structural heterogeneities within multilayered membranes to induce inhomogeneous straining, providing additional design freedom in engineering the mechanical strain within the membrane, and in turn the possibility to achieve a higher level of manipulation over the rollup geometry [40–44]. For instance, alternative strips with varied chemical compositions have been utilized to construct the responsive material with local modulation of internal stress that enables controllable multiple 3D geometry transformations from self-bending to self-twisting [45]. Aligned carbon nanotubes (CNTs) in multiple directions have been reported to be embedded into the composite polymer membrane actuators to realize the accurate control of the self-rolling process and thus endow programmable and anisotropic actuation [46]. One of the most significant features offered by those inhomogeneously strained structures is the directional self-rolling behaviors originating from anisotropic driving forces [47], greatly enriching the flexibility and tunability in 3D architectures constructed from predefined flat geometries.

The added compositional and structural heterogeneities, despite the benefits, also bring along challenges for quantitative assessment of the rolling process. The theoretical models [47–49] available demonstrate the ability of design helical ribbons through compositional inhomogeneity but fail to analytically evaluate the two unequal principal curvatures of strained bilayer membranes induced structural and compositional inhomogeneity. Moreover, experimental measurements are still needed to obtain those values for the precise design of various 3D morphologies [47]. As such, there is need of predictive and quantitative models that account for material heterogeneity in the strained membranes.

This present study aims to address the afore-mentioned knowledge deficit. An analytical model has been established to predict self-rolling curvatures of strained bilayer membranes incorporating heterogeneous elements. Molecular dynamics (MD) simulations, on the heterogeneous $CdTe_xS_{1-x}$/CdTe bilayer system, were performed to directly examine the rolling behaviors to validate the analytical model. Moreover, numerical simulations

* Corresponding author.
E-mail address: jun.song2@mcgill.ca (J. Song).

https://doi.org/10.1016/j.eml.2019.100451
2352-4316/

using finite-element modeling (FEM) were performed to examine the role of heterogeneous elements in the complex helical rolling, and to further demonstrate the application of the analytical model. In the end, a summary was presented and the implication of our results to the design of complex 3D structures based on strained membranes was discussed.

2. Methodology

2.1. Analytical formulation

Fig. 1 schematically illustrates the representative strained bilayer membrane, where a rectangular strained bilayer membrane has been considered with dimensions L in length (x_1 direction) and W in width (x_2 direction), comprising an mixed active layer with aligned heterogeneous elements (top layer) and a passive matrix layer (bottom layer) bonded together. The lattice constants of matrix and two heterogeneous materials are expressed by a_s, a_{f1} and a_{f2}, respectively. Here subscripts s, $f1$ and $f2$ denote the matrix in red and two types of heterogeneous materials in yellow and blue, respectively, and we continue to use this notation in the following text.

The two types of heterogeneous materials, and matrix are respectively of elastic constants (C_{11f1}, C_{12f1}, C_{44f1}), (C_{11f2}, C_{12f2}, C_{44f2}), (C_{11s}, C_{12s}, C_{44s}), and thicknesses ($h_{f1} = h_{f2}$, h_s), where both materials are assumed to be cubic symmetrical. Then, the elastic modulus of mixed top layer with the subscript fx could be expressed using a weighted mean as

$$C_{11fx} = F \cdot C_{11f1} + C_{11f2} \cdot (1 - F) \tag{1}$$

$$C_{12fx} = F \cdot C_{12f1} + C_{11f2} \cdot (1 - F) \tag{2}$$

$$C_{44fx} = F \cdot C_{44f1} + C_{11f2} \cdot (1 - F) \tag{3}$$

where F is the volume fraction of heterogeneous elements. The variation of internal strain induced by aligned heterogeneous elements is systematically examined using continuum elastic theory. The deformation process is schematically illustrated in Fig. 1(b). The heterogeneous elements, bonded together and adhered to the matrix, stretch or contract, both longitudinally (along x_1) and laterally (along x_2), to match the matrix. Here it is assumed that the matrix and heterogeneous elements deform in a way to ensure an even outer surface in the equilibrium state. The in plane anisotropic mismatch strains ($\varepsilon_{\parallel}$, $\varepsilon_{\perp}$), parallel and perpendicular to the direction of aligned heterogeneous elements can then be determined as the following, based on the lattice constants of matrix and heterogeneous material (see Eqs. (4) and (5) given in Box I. with coefficients $\boldsymbol{M}$ and $\boldsymbol{N}$ given by

$$\boldsymbol{M} = \frac{C_{12f1}a_{f1}\left(C_{11f2}^2 - C_{12f2}^2\right)\left(a_{f2} - a_{f1}\right)(1-F)F}{C_{11f1}^2 C_{11f2}a_{f2}F - C_{11f1}\left(C_{11f2}^2 - C_{12f2}^2\right)(F-1)a_{f1} - C_{11f2}C_{12f1}^2 a_{f2}F} \tag{6}$$

$$\boldsymbol{N} = \frac{C_{12f2}a_{f2}\left(C_{11f1}^2 - C_{12f1}^2\right)\left(a_{f2} - a_{f1}\right)(1-F)F}{C_{11f1}^2 C_{11f2}a_{f2}F - C_{11f1}\left(C_{11f2}^2 - C_{12f2}^2\right)(F-1)a_{f1} - C_{11f2}C_{12f1}^2 a_{f2}F} \tag{7}$$

For the sake of simplicity and without loss the generality, we assume one type of the heterogeneous elements are of the same material as the substrate, colored in yellow and red in Fig. 1, respectively, i.e., $a_{f2} = a_s$, $C_{11f2} = C_{11s}$, $C_{12f2} = C_{12s}$, $C_{44f2} = C_{44s}$. As to be shown below, analytical solutions are possible under this assumption.

Then Eqs. (4)–(7) can then be further reduced as:

$$\varepsilon_{\parallel} = \frac{C_{11s}F\left(C_{11f}^2 - C_{12f}^2\right)\left(a_s - a_f\right)}{a_f\left(C_{11f}^2 C_{11s}F - \left(C_{11s}^2 - C_{12s}^2\right)(F-1)C_{11f} - C_{12f}^2 C_{11s}F\right)} \tag{8}$$

$$\varepsilon_{\perp} = \frac{a_s}{a_s + \left(a_s - a_f\right)F - \boldsymbol{M} + \boldsymbol{N}} - 1 \tag{9}$$

$$\boldsymbol{M} = \frac{C_{12f}a_f\left(C_{11s}^2 - C_{12s}^2\right)\left(a_s - a_f\right)(1-F)F}{C_{11s}a_s(C_{11f}^2 - C_{12f}^2)F - C_{11f}\left(C_{11s}^2 - C_{12s}^2\right)(F-1)a_f} \tag{10}$$

$$\boldsymbol{N} = \frac{C_{12s}a_s\left(C_{11f}^2 - C_{12f}^2\right)\left(a_s - a_f\right)(1-F)F}{C_{11s}a_s(C_{11f}^2 - C_{12f}^2)F - C_{11f}\left(C_{11s}^2 - C_{12s}^2\right)(F-1)a_f} \tag{11}$$

The relations of strain tensor $\varepsilon_{\alpha\beta}$ and displacement fields $\boldsymbol{u}(u_1, u_2, u_3)$ of the deformed membranes are evaluated in a given coordinate (x_1, x_2, x_3) based on the Von-Karman nonlinear theory [50,51],

$$\varepsilon_{\alpha\beta} = \frac{1}{2}\left(\frac{\partial u_\alpha}{\partial x_\beta} + \frac{\partial u_\beta}{\partial x_\alpha} + \frac{\partial u_3}{\partial x_\beta}\cdot\frac{\partial u_3}{\partial x_\alpha}\right) - x_3\frac{\partial^2 u_3}{\partial x_\alpha \partial x_\beta} \tag{12}$$

where the Greek subscripts α and β can have values 1 or 2. An approximated displacement field [50,52–54], could be assumed as

$$u_1(x_1, x_2) = \sum_{i=0}^{3}\sum_{j=0}^{3} A_{ij}x_1^i x_2^j, \tag{13}$$

$$u_2(x_1, x_2) = \sum_{i=0}^{3}\sum_{j=0}^{3} B_{ij}x_1^i x_2^j, \tag{14}$$

$$u_3 = \frac{1}{2}\left(ax_1^2 + bx_2^2\right), \tag{15}$$

where (A_{ij}, B_{ij}, a, and b) are to-be-determined coefficients minimizing the potential energy $\boldsymbol{U}$ (see below). Here the three-order polynomial approximation of in-plane displacement field was proved to be sufficient to provide an accurate estimation for the self-rolling behaviors of strained bilayer membranes with inhomogeneous elements. From the displacement fields, the curvature fields of the deformed membranes can then be obtained:

$$\kappa_{11} = \frac{\partial^2 u_3}{\partial x_1^2} \text{ and } \kappa_{22} = \frac{\partial^2 u_3}{\partial x_2^2} \tag{16}$$

The total potential energy $\boldsymbol{U}$ of the bilayer membrane system follows by integrating the strain energy over the total volume as

$$U = \iiint_V \left(\frac{1}{2}C_{ijkl}^S \varepsilon_{ij}^S \varepsilon_{kl}^S + \frac{1}{2}C_{ijkl}^{fx}\varepsilon_{ij}^{fx}\varepsilon_{kl}^{fx}\right)dV \tag{17}$$

where, C_{ijkl}^S and C_{ijkl}^{fx} are the stiffness tensors for the matrix and the materials in the heterogeneous top layer, respectively. The equilibrium configurations can be obtained via minimization of the total potential energy expression based on the trial in-plane displacement functions and transverse displacement shape functions. It is worth noting that in this quasi-static process, there can be multi-stable equilibrium states, including the situations with two unequal final curvatures and with one principal curvature, as demonstrated by numerical simulations in our previous study [55]. We found that the closed analytical solutions are only available for the case of one principal curvature, as shown in Eqs. (18) and (19) which is given in Box II, where $CF_1 = \frac{C_{11f1}^2 - C_{12f1}\cdot C_{12f1}}{C_{11f1}}$, $CF_2 = \frac{C_{12f1}\cdot(C_{11f1} - C_{12f1})}{C_{11f1}}$, $CS_1 = \frac{C_{11s}^2 - C_{12s}^2}{C_{11s}}$ and $CS_2 = \frac{C_{12s}\cdot(C_{11s} - C_{12s})}{C_{11s}}$.

2.2. Molecular dynamics simulations

To validate the curvature predictions from the continuum model in Section 2.1 and directly visualize the self-rolling behaviors, we performed molecular dynamics (MD) simulations implemented using the LAMMPS package [56]. Here in this study the $CdTe_xS_{1-x}$/CdTe bilayer is selected as the representative model system, with $CdTe_xS_{1-x}$ and CdTe denoting the materials for the

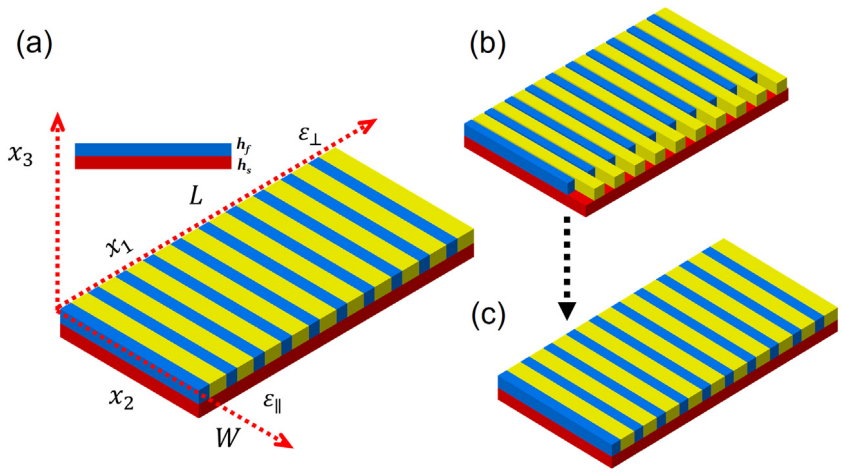

Fig. 1. (a) Exaggerated schematic illustration of rectangular strained bilayer membrane with aligned heterogeneous elements colored in the blue and yellow. (b) The matrix and heterogeneous material in the strain-free state prior to being bonded together. (c) The heterogeneous material is stretched and bonded with the matrix and two materials contract the same amount and obtain even outer surface in the equilibrium state. Note that in the study heterogeneous elements may align along either x_1 or x_2, although here only the case of alignment along x_2 is illustrated. (For interpretation of the references to color in this figure legend, the reader is referred to the web version of this article.)

$$\varepsilon_\parallel = \frac{a_{f2}FC_{11f2}C_{11f1}^2\left(a_s-a_{f1}\right)-a_{f1}C_{11f1}\left(C_{11f2}^2-C_{12f2}^2\right)(F-1)\left(a_s-a_{f2}\right)-a_{f2}FC_{11f2}C_{12f1}^2\left(a_s-a_{f1}\right)}{a_{f1}a_{f2}\left(C_{11f1}^2C_{11f2}F-\left(C_{11f2}^2-C_{12f2}^2\right)(F-1)C_{11f1}-C_{12f1}^2C_{11f2}F\right)} \tag{4}$$

$$\varepsilon_\perp = \frac{a_s}{a_s+\left(a_s-a_{f1}\right)F-\boldsymbol{M}+\boldsymbol{N}}-1 \tag{5}$$

Box I.

$$\frac{1}{k_{11}} = \left[\frac{\left(CF_1^3-CF_1CF_2^2\right)h_f^5+5h_s\left(CF_1^2CS_1-\frac{2}{5}CF_1CF_2CS_2-\frac{3}{5}CF_2^2CS_1\right)h_f^4+6h_s^2\left(CF_1^2CS_1+\left(\frac{2}{3}CS_1^2-\frac{2}{3}CS_2^2\right)CF_1-CF_2^2CS_1\right)h_f^3}{6h_s\left(h_s+h_f\right)h_f\left(\left(CF_1^2-CF_2^2\right)\left(CS_1\varepsilon_\parallel+CS_2\varepsilon_\perp\right)h_f+h_s\left(CS_1^2-CS_2^2\right)\left(CF_1\varepsilon_\parallel+CF_2\varepsilon_\perp\right)\right)}\right. \\ \left.+\frac{4h_s^3\left(CF_1^2CS_1+\left(\frac{3}{2}CS_1^2-\frac{3}{2}CS_2^2\right)CF_1-CF_2^2CS1\right)h_f^2+5h_s^4\left(\left(CS_1^2-\frac{3}{5}CS_2^2\right)CF_1-\frac{2}{5}CF_2CS_1CS_2\right)h_f+\left(CS_1^3-CS_1CS_2^2\right)h_s^5}{6h_s\left(h_s+h_f\right)h_f\left(\left(CF_1^2-CF_2^2\right)\left(CS_1\varepsilon_\parallel+CS_2\varepsilon_\perp\right)h_f+h_s\left(CS_1^2-CS_2^2\right)\left(CF_1\varepsilon_\parallel+CF_2\varepsilon_\perp\right)\right)}\right] \tag{18}$$

$$\frac{1}{k_{22}} = \left[\frac{\left(CF_1^3-CF_1CF_2^2\right)h_f^5+5h_s\left(CF_1^2CS_1-\frac{2}{5}CF_1CF_2CS_2-\frac{3}{5}CF_2^2CS_1\right)h_f^4+6h_s^2\left(CF_1^2CS_1+\left(\frac{2}{3}CS_1^2-\frac{2}{3}CS_2^2\right)CF_1-CF_2^2CS_1\right)h_f^3}{6h_s\left(h_s+h_f\right)h_f\left(\left(CF_1^2-CF_2^2\right)\left(CS_1\varepsilon_2+CS_2\varepsilon_\parallel\right)h_f+h_s\left(CS_1^2-CS_2^2\right)\left(CF_1\varepsilon_2+CF_2\varepsilon_\parallel\right)\right)}\right. \\ \left.+\frac{4h_s^3\left(CF_1^2CS_1+\left(\frac{3}{2}CS_1^2-\frac{3}{2}CS_2^2\right)CF_1-CF_2^2CS1\right)h_f^2+5h_s^4\left(\left(CS_1^2-\frac{3}{5}CS_2^2\right)CF_1-\frac{2}{5}CF_2CS_1CS_2\right)h_f+\left(CS_1^3-CS_1CS_2^2\right)h_s^5}{6h_s\left(h_s+h_f\right)h_f\left(\left(CF_1^2-CF_2^2\right)\left(CS_1\varepsilon_\perp+CS_2\varepsilon_\parallel\right)h_f+h_s\left(CS_1^2-CS_2^2\right)\left(CF_1\varepsilon_\perp+CF_2\varepsilon_\parallel\right)\right)}\right] \tag{19}$$

Box II.

top mixed layer and substrate layer respectively. This choice is based on the availability of interatomic potential [57], and the practical implication as the quasi-two-dimensional morphologies of $CdTe_xS_{1-x}$ and CdTe are promising building blocks for tunable optoelectronic devices [58,59]. The interatomic interactions of the Cd–S–Te ternary system are described by the Stillinger–Weber potential [57], which well predicts the lattice parameter, elastic constants and a wide variety of defect properties for bulk and multilayered compounds, and has been previously applied to study core/shell structured quantum dots [60], misfit dislocations [61], and heterogeneous film growth [62]. The lattice constants and elastic constants of CdS and CdTe, predicted by the interatomic potential, are listed in Table 1. The effective Young's moduli, evaluated based on the Voigt average [63], are also listed in Table 1.

The initial atomistic models and the corresponding MD simulated rolling processes are illustrated in Fig. 2(a-d), where x_1 (perpendicular to the plane of paper), x_2, and x_3 are set to be aligned with [100], [010], and [001] respectively, and the periodic boundary condition is applied to x_1 direction. The supercell dimensions along x_1 and x_2 are approximately 28 nm and 110 nm respectively. As illustrated in Fig. 2(a-b), the top layer comprises of alternating CdS and CdTe strips, along either the longitudinal or lateral direction. For each strip type (CdS or CdTe), the strips are of the same strip width, and spatial strip density, defined as # of strips per length along the direction perpendicular to the strip, is maintained to be sufficient (>0.5/nm), in order to

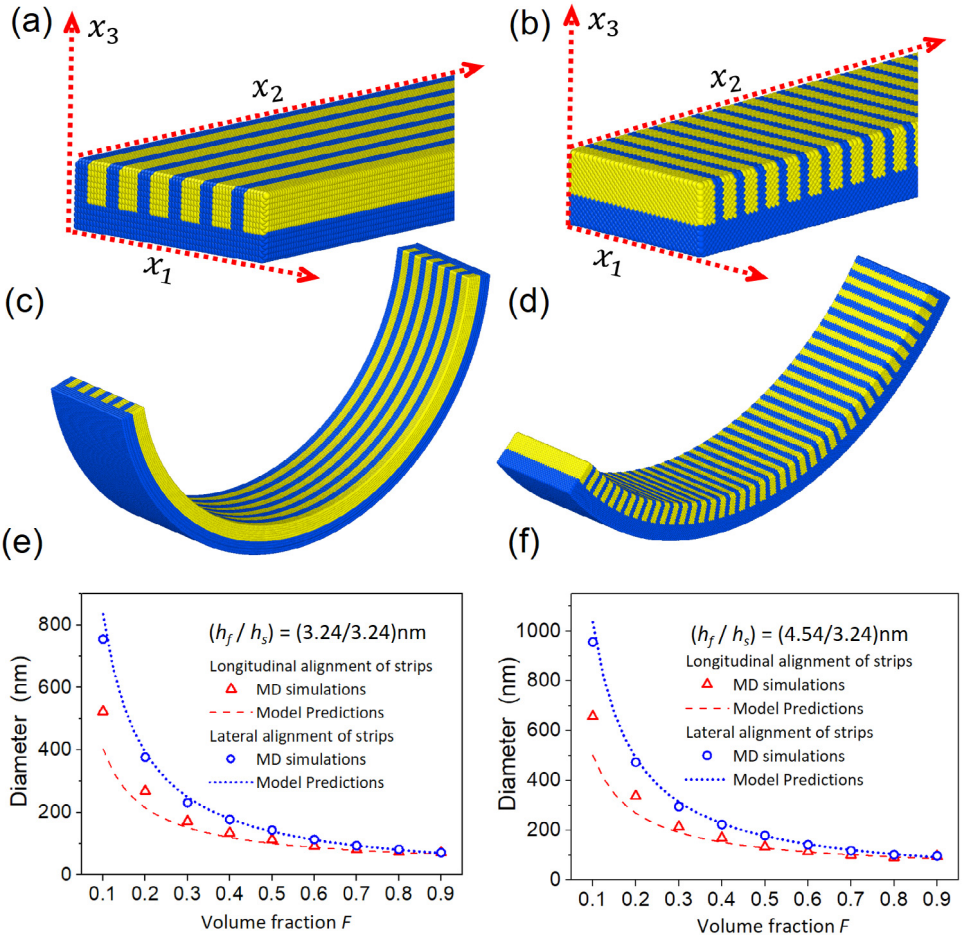

Fig. 2. Representative self-rolling models of $CdTe_xS_{1-x}$/CdTe of volume fraction 0.6 with alternatingly distributed strips in the top layer aligned along the (a) longitudinal and (b) lateral directions, while (c) and (d) represent the corresponding equilibrium rollup geometries. The MD simulated and model predicted rollup diameters as functions of the volume fraction (F) of the active material CdS for two representative sets of layer thicknesses, i.e., (h_f/h_s) being (3.24/3.24) and (4.54/3.24) nm are shown in (e) and (f) respectively.

ensure adequate level of uniformity in material responses for the mixed top layer (see Supplementary Information for details). The $CdTe_xS_{1-x}$/CdTe bilayer systems of two sample set of thicknesses, i.e., (h_f/h_s) being (3.24/3.24) and (3.24/4.54) nm were considered to investigate the thickness effect on the rollup. In MD simulations, the lattice of the top layer was first stretched to match that of the matrix CdTe. Then the heterogeneous strained bilayer was relaxed via energy minimization [64] to obtain the equilibrium rollup structure. After the relaxation, the rolling diameter is measured at the mid-plane of $CdTe_xS_{1-x}$/CdTe system. In addition to the above atomistic models where CdS were embedded in the top layer as heterogeneous strips, we also consider two additional cases, one with the top layer being pure CdS while the other with the top layer being homogeneously mixed $CdTe_xS_{1-x}$ (see Supplementary Information for details).

2.3. Numerical simulations

For larger-scale rollup and more complex rollup geometries (e.g., helical) that involve competitive rolling behaviors, they are beyond the reach of MD simulations, and consequently numerical simulations using finite element modeling (FEM) were used, implemented by the ABAQUS package [65]. The layered structures with predefined inhomogeneous strips were built in the module of composite layups, and 4-node doubly curved thin/thick shell elements with reduced integration (S4R) were used to discretize the shell geometry. The initial lattice mismatch strain was realized through setting different thermal expansion coefficients for each layer with controllable temperature variation. ABAQUS explicit/dynamic package was employed to examine the self-rolling behaviors of membranes with strip heterogeneous elements embedded. No pre-constrain was imposed to influence the rollup direction corresponding to the situation of isotropic etching release.

Table 1
The values of lattice constants (a) and elastic constants (C_{11}, C_{12}, C_{44}) obtained through the MD simulations at 0 K, and the derived Voight averaged Young's modulus and Poisson's ratio [63].

Material	C_{11} (GPa)	C_{12} (GPa)	C_{44} (GPa)	E (GPa)	ν	a (nm)
CdS	108	37.5	46.6	102.6	0.22	0.5835
CdTe	64	33	23	52	0.3	0.6413

3. Results and discussions

The MD simulated rollup configurations with the CdS strips aligned along the longitude and lateral directions are illustrated in Fig. 2(c) and (d) respectively. The simulated rollup diameters as the volume fraction F of the active material CdS varies for two representative sets of layer thicknesses, i.e., (h_f/h_s) being

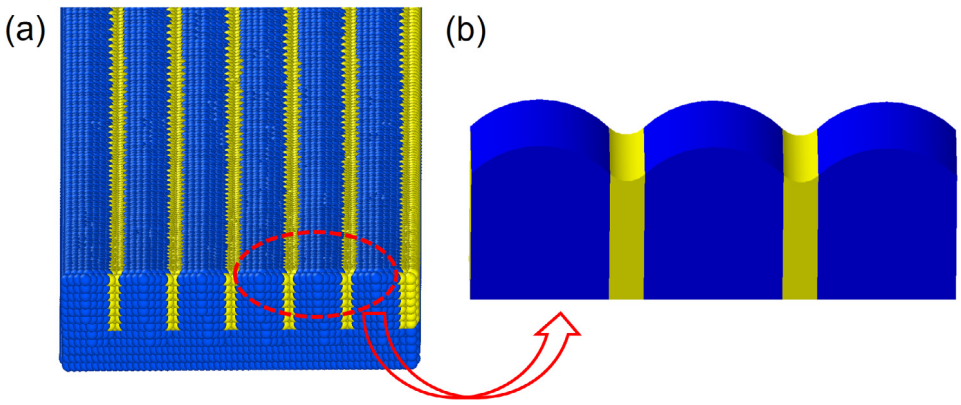

Fig. 3. (a) The (partial) atomic configuration of an example heterogeneous bilayer configuration of longitudinal alignment of strips with small $F = 0.2$, where a curved outer surface can be observed, with the surface grooving exaggerated in the schematic view in (b).

(3.24/3.24) and (4.54/3.24) nm are listed in Fig. 2(e) and (f) respectively. With increasing volume fraction that gives rise to more lattice mismatch, the rollup diameter (curvature) decreases (increases) as expected. Our results also reveal that the longitudinal strip alignment leads to smaller rollup diameter compared to that from lateral strip alignment with the same volume fraction, indicative of more driving force produced by longitudinal alignment, which is likely due to anisotropy in elastic constants. In addition, increase in the thickness ratio h_f/h_s also results in larger rollup diameters. Comparing the simulation results with the continuum model predictions in Fig. 2, we see that overall good agreement is achieved. Deviation between MD simulation and continuum model prediction starts to appear for small volume fracture, e.g., for $F < 0.3$ in the case of longitudinal alignment of strips, the model prediction underestimates the rollup diameter. Such deviation can be attributed to surface grooving induced strain relief at interfaces between strips, as illustrated in Fig. 3. Actually, our theoretical predictions are based on the assumption that when the matrix and heterogeneous elements are bonded together, they would contract the same amount along the longitudinal direction and obtain even outer surface. However, it is no longer the real case when surface grooving happens, and the mismatch strain along longitudinal direction would be released, resulting in larger rollup diameters.

Further to the simple rollup structures examined by the MD simulations, the role of heterogeneous elements in the formation of the more complex self-rolling geometries, i.e., helical shapes, were investigated using FEM simulations. The FEM model is schematically illustrated in Fig. 4(a) where helical formation from a starting parallelogram bilayer membrane of dimensions of 8 μm $\times$ 40 μm with a designed helical angle $\alpha = 26^\circ$ and a fixed $h_s = 25$ nm was considered. The heterogeneous elements were taken to be aligned parallel to the short edge of the parallelogram. The volume fraction F and minimum strip width are taken to be 0.5 and 0.1 μm, respectively. Then the corresponding lattice mismatch is realized by setting different thermal expansion coefficients for different components with desired temperature variations. With the volume fraction fixed, the lattice mismatch is determined and specified by the lattice constants of CdTe and CdS. However, we allow the elastic constants of the heterogeneous elements to vary, rather than being limited to the $CdTe_xS_{1-x}$, which would enable us to extend the investigation beyond $CdTe_xS_{1-x}$/CdTe material system. Specifically, we allow the ratio of difference in elastic constants, defined as $\Delta(=(E_{f1}-E_s)/E_s)$ to vary between -1 to 1 (note $CdTe_xS_{1-x}$/CdTe would only allow Δ to vary in the range of [0, 1]). Meanwhile we also vary the height of the top layer h_f.

The rolling behaviors and resultant helical geometries were then examined. As illustrated in Fig. 4, different helical rolling behaviors can be achieved depending on the combination of Δ and h_f. In particular, when (Δ, h_f) fall into certain regimes, there exist two well-defined, distinct rolling modes, with the rolling direction parallel (Mode I) or perpendicular (Mode II) to the aligned direction of heterogeneous elements, while otherwise the rolling direction/geometry is not well defined. Here, a rollup configuration is considered "not defined" when the helix shows non-straight axis (i.e., there is no well-defined helix axis) and spatially varying curvature (see Supplementary Information for details). From Fig. 4, we see that the occurrence of Mode I or Mode II rolling is strongly dependent on Δ, i.e., Mode I and Mode II are induced in regimes where Δ assumes large positive and negative values respectively. This suggests that Mode I necessitate stiffer heterogeneous elements than the matrix while Mode II require the opposite. Meanwhile, we see that the threshold Δ to trigger Mode I rolling shows a non-monotonic dependence of the top layer thickness h_f. This non-monotonic response can be attributed to the competitive balance between higher driving force for rolling and larger bending stiffness, as the top layer thickness increases, where, the local minimum in both cases indicates the point where the benefit from the increased driving force of thicker active layer is offset by the loss of increased bending stiffness of increased thickness. But for Mode II, increased top layer thicknesses require larger threshold Δ values, which means no local equilibrium could be achieved for the increased driving force and larger bending stiffness. The competition between Mode I and Mode II as Δ varies may also be further analyzed through examining the corresponding equilibrium strain energies of the rollup structure (see Supplementary Information for details).

For cases of helical rolling falling into the regimes of Mode I and Mode II, the helix configuration is well defined, and the helix diameter is measured. Meanwhile, the helix diameter is assumed to be same as the normal rollup diameter and thus can also be predicted based on Eqs. (13)–(16). The model predicted helix diameters (D_{Helix}^{Pred}) are compared with the FEM simulated ones (D_{Helix}^{FEM}) in Fig. 4(c), for a few sample cases of Mode I or Mode II rolling, showing excellent agreement, which further evidences the accuracy of the analytical model. Figs. 2 and 4 together demonstrate that it is possible to predictively tune both the rolling direction and rollup curvature by modulating the material heterogeneity. It is also worth noting that the theoretical framework developed is size and material independent, and may be readily extended to examine the self-rolling behaviors of systems of more complex architectures and/or material responses (see Supplementary Information for additional details).

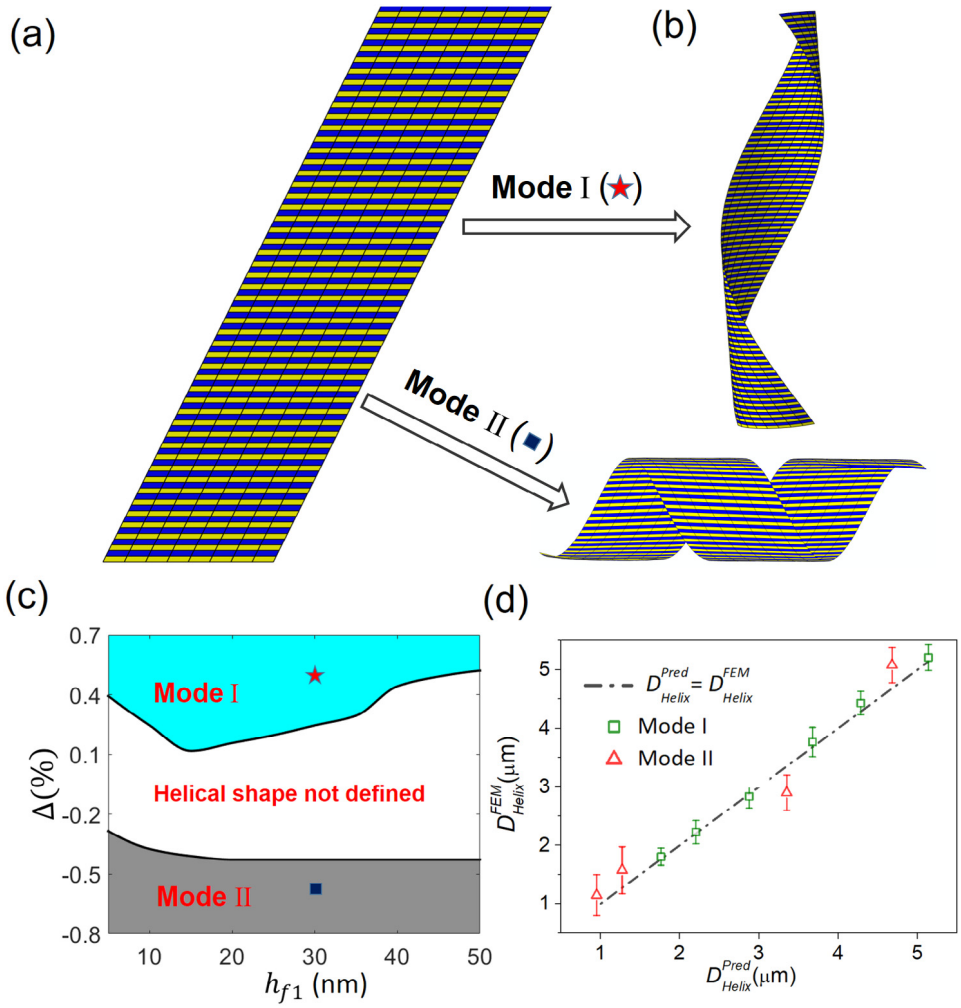

Fig. 4. (a) FE simulated helical rolling processes of the bilayer of $CdTe_xS_{1-x}$/CdTe with alternative distributed heterogeneous strips of volume fraction 0.5 where two distinct rolling modes (Mode I and Mode II) are observed. The occurrence of these two modes depends on $\Delta(=(\boldsymbol{E_{f1}}-\boldsymbol{E_s})/\boldsymbol{E_s})$ and $\boldsymbol{h_{f1}}$, as illustrated in (b), where the light cyan and light gray regions correspond to Mode I and Mode II occurring, while the white region corresponds to the situation when no well-defined helical shape is formed from rolling. (c) Comparison of the model predicted helix diameters ($\boldsymbol{D^{Pred}_{Helix}}$) from Eqs. (13)–(16) and the FEM simulated ones ($\boldsymbol{D^{FEM}_{Helix}}$) for a few sample cases of helixes, being either Mode I or Mode II, obtained at different (Δ, $\boldsymbol{h_{f1}}$) combinations, where the symbols denote FEM data.

4. Conclusion

In summary, we presented a comprehensive theoretical study of the effects of material heterogeneity on self-rolling of strained membranes. An analytical model has been established to predict self-rolling curvatures of strained bilayer membranes, accounting for material heterogeneity and strain anisotropy. The accuracy of our model is validated through molecular dynamics (MD) simulations on the $CdTe_xS_{1-x}$/CdTe bilayer system. Further to MD simulations, numerical simulations using finite-element modeling (FEM) have been performed to examine the role of heterogeneous elements in the complex helical rolling. It has been demonstrated that different helical rolling modes can be induced by modulating the material heterogeneity and layer thickness, with the resultant helix diameter well predicted by the analytical model. The present study offers new thoughts towards predictive design and tuning of complex 3D structures based on strained membranes.

Acknowledgments

We greatly thank the financial support from McGill Engineering Doctoral Award, China Scholarship Council, National Sciences and Engineering Research Council (NSERC) Discovery grant (grant # RGPIN-2017-05187), and NSERC Strategic grant (grant # STPGP 494012-16). We also acknowledge Supercomputer Consortium Laval UQAM McGill and Eastern Quebec for providing computing power.

Appendix A. Supplementary data

Supplementary material related to this article can be found online at https://doi.org/10.1016/j.eml.2019.100451.

References

[1] Y.H. Zhang, F. Zhang, Z. Yan, Q. Ma, X.L. Li, Y.G. Huang, J.A. Rogers, Nat. Rev. Mater. 2 (2017).
[2] L.Z. Xu, T.C. Shyu, N.A. Kotov, Acs Nano 11 (2017) 7587.
[3] H.J. Bae, S. Bae, J. Yoon, C. Park, K. Kim, S. Kwon, W. Park, Sci. Adv. 3 (2017).
[4] Y. Wang, Z.W. Li, J.L. Xiao, J. Electron. Packag. 138 (2016).
[5] S. Xu, Z. Yan, K.I. Jang, W. Huang, H.R. Fu, J. Kim, Z. Wei, M. Flavin, J. McCracken, R. Wang, A. Badea, Y. Liu, D.Q. Xiao, G.Y. Zhou, J. Lee, H.U. Chung, H.Y. Cheng, W. Ren, A. Banks, X.L. Li, U. Paik, R.G. Nuzzo, Y.G. Huang, Y.H. Zhang, J.A. Rogers, Science 347 (2015) 154.
[6] Z. Yan, F. Zhang, F. Liu, M.D. Han, D.P. Ou, Y.H. Liu, Q. Lin, X.L. Guo, H.R. Fu, Z.Q. Xie, M.Y. Gao, Y.M. Huang, J. Kim, Y.T. Qiu, K.W. Nan, J. Kim, P. Gutruf, H.Y. Luo, A. Zhao, K.C. Hwang, Y.G. Huang, Y.H. Zhang, J.A. Rogers, Sci. Adv. 2 (2016).

[7] O.V. Cangellaris, E.A. Corbin, P. Froeter, J.A. Michaels, X.L. Li, M.U. Gillette, ACS Appl. Mater. Interfaces 10 (2018) 35705.
[8] Z. Tian, W. Huang, B.R. Xu, X.L. Li, Y.F. Mei, Nano Lett. 18 (2018) 3688.
[9] R. Sharma, C.C.B. Bufon, D. Grimm, R. Sommer, A. Wollatz, J. Schadewald, D.J. Thurmer, P.F. Siles, M. Bauer, O.G. Schmidt, Adv. Energy Mater. 4 (2014).
[10] Y.F. Mei, G.S. Huang, A.A. Solovev, E.B. Urena, I. Moench, F. Ding, T. Reindl, R.K.Y. Fu, P.K. Chu, O.G. Schmidt, Adv. Mater. 20 (2008) 4085.
[11] D. Grimm, R.B. Wilson, B. Teshome, S. Gorantla, M.H. Rummeli, T. Bublat, E. Zallo, G.D. Li, D.G. Cahill, O.G. Schmidt, Nano Lett. 14 (2014) 2387.
[12] J.W. Deng, X.Y. Lu, L.X. Liu, L. Zhang, O.G. Schmidt, Adv. Energy Mater. 6 (2016).
[13] Q.T. Zhang, J. Wommer, C. O'Rourke, J. Teitelman, Y.C. Tang, J. Robison, G.J. Lin, J. Yin, Extreme Mech. Lett. 11 (2017) 111.
[14] Y. Shi, F. Zhang, K.W. Nan, X.J. Wang, J.T. Wang, Y.J. Zhang, Y.T. Zhang, H.W. Luan, K.C. Hwang, Y.G. Huang, J.A. Rogers, Y.H. Zhang, Extreme Mech. Lett. 15 (2017) 151.
[15] Z. Yan, M.D. Han, Y.Y. Yang, K.W. Nan, H.W. Luan, Y.Y. Luo, Y.H. Zhang, Y.G. Huang, J.A. Rogers, Extreme Mech. Lett. 11 (2017) 96.
[16] D. a. Grimm, Nano Lett. 13 (2013) 213.
[17] E.J. Smith, S. Schulze, S. Kiravittaya, Y. Mei, S. Sanchez, O.G. Schmidt, Nano Lett. 11 (2011) 4037.
[18] I. Mnch, D. Makarov, R. Koseva, L. Baraban, D. Karnaushenko, C. Kaiser, K.F. Arndt, O.G. Schmidt, ACS Nano 5 (2011) 7436.
[19] J.J. Abbott, K.E. Peyer, L.X.X. Dong, B.J. Nelson, Robot. Res. 66 (2010) 157.
[20] J.J. Abbott, K.E. Peyer, M.C. Lagomarsino, L. Zhang, L.X. Dong, I.K. Kaliakatsos, B.J. Nelson, Int. J. Robot. Res. 28 (2009) 1434.
[21] R. Arayanarakool, A.K. Meyer, L. Helbig, S. Sanchez, O.G. Schmidt, Lab Chip 15 (2015) 2981.
[22] R. Fernandes, D.H. Gracias, Adv. Drug Deliv. Rev. 64 (2012) 1579.
[23] S.M. Harazim, V.A.B. Quinones, S. Kiravittaya, S. Sanchez, O.G. Schmidt, Lab Chip 12 (2012) 2649.
[24] A. Bernardi, S. Kiravittaya, A. Rastelli, R. Songmuang, D.J. Thurmer, M. Benyoucef, O.G. Schmidt, Appl. Phys. Lett. 93 (2008) 094106.
[25] S.M. Harazim, W. Xi, C.K. Schmidt, S. Sanchez, O.G. Schmidt, J. Mater. Chem. 22 (2012) 2878.
[26] W. Huang, J.C. Zhou, P.J. Froeter, K. Walsh, S.Y. Liu, M.D. Kraman, M.Y. Li, J.A. Michaels, D.J. Sievers, S.B. Gong, X.L. Li, Nat. Electron. 1 (2018) 305.
[27] K.U. Jeong, J.H. Jang, D.Y. Kim, C. Nah, J.H. Lee, M.H. Lee, H.J. Sun, C.L. Wang, S.Z.D. Cheng, E.L. Thomas, J. Mater. Chem. 21 (2011) 6824.
[28] L. Ionov, Adv. Funct. Mater. 23 (2013) 4555.
[29] L. Persano, A. Camposeo, D. Pisignano, J. Mater. Chem. C 1 (2013) 7663.
[30] R. Kempaiah, Z.H. Nie, J. Mater. Chem. B 2 (2014) 2357.
[31] M. Podgorski, D.P. Nair, S. Chatani, G. Berg, C.N. Bowman, ACS Appl. Mater. Interfaces 6 (2014) 6111.
[32] A.R. Studart, Angew. Chem. Int. Edn 54 (2015) 3400.
[33] F.M. Wisser, B. Schumm, G. Mondin, J. Grothe, S. Kaskel, J. Mater. Chem. C 3 (2015) 2717.
[34] A.S. Gladman, E.A. Matsumoto, R.G. Nuzzo, L. Mahadevan, J.A. Lewis, Nature Mater. 15 (2016) 413.
[35] S. Coyle, C. Majidi, P. LeDuc, K.J. Hsia, Extreme Mech. Lett. 22 (2018) 51.
[36] T. Sakanoue, M. Mizukami, S. Oku, Y. Yoshimura, M. Abiko, S. Tokito, Appl. Phys. Express 7 (2014).
[37] R. Garcia, A.W. Knoll, E. Riedo, Nature Nanotechnol. 9 (2014) 577.
[38] J.K.Y. Ong, D. Moore, J. Kane, R.F. Saraf, ACS Appl. Mater. Interfaces 6 (2014) 14278.
[39] H. Schift, Appl. Phys. A 121 (2015) 415.
[40] Q. Ge, H.J. Qi, M.L. Dunn, Appl. Phys. Lett. 103 (2013).
[41] S. Janbaz, R. Hedayati, A.A. Zadpoor, Mater. Horiz. 3 (2016) 536.
[42] Y.Q. Mao, Z. Ding, C. Yuan, S.G. Ai, M. Isakov, J.T. Wu, T.J. Wang, M.L. Dunn, H.J. Qi, Sci. Rep. 6 (2016).
[43] J. Zhou, S.S. Sheiko, J. Polym. Sci. Part B 54 (2016) 1365.
[44] O. Kuksenok, A.C. Balazs, Mater. Horiz. 3 (2016) 53.
[45] Z.L. Wu, M. Moshe, J. Greener, H. Therien-Aubin, Z.H. Nie, E. Sharon, E. Kumacheva, Nature Commun. 4 (2013).
[46] H. Lin, J. Gong, M. Eder, R. Schuetz, H. Peng, J.W.C. Dunlop, J. Yuan, Adv. Mater. Interfaces 1600768 (2016).
[47] X.J. Yu, L.N. Zhang, N. Hu, H. Grover, S.C. Huang, D. Wang, Z. Chen, Appl. Phys. Lett. 110 (2017).
[48] Q. Guo, A.K. Mehta, M.A. Grover, W. Chen, D.G. Lynn, Z. Chen, Appl. Phys. Lett. 104 (2014).
[49] Z. Chen, C. Majidi, D.J. Srolovitz, M. Haataja, Appl. Phys. Lett. 98 (2011).
[50] A.F. Bower, Applied Mechanics of Solids, CRC Press, 2009.
[51] O.A. Bauchau, J.I. Craig, in: O.A. Bauchau, J.I. Craig (Eds.), Structural Analysis, Springer Netherlands, Dordrecht, 2009, p. 819.
[52] S. Vidoli, Int. J. Solids Struct. 50 (2013) 1241.
[53] M.L. Dano, M.W. Hyer, Int. J. Solids Struct. 35 (1998) 2101.
[54] M.W. Hyer, J. Compos. Mater. 15 (1981) 296.
[55] C. Chen, P.F. Song, F.C. Meng, X. Li, X.Y. Liu, J. Song, Nanotechnology 28 (2017).
[56] S. Plimpton, J. Comput. Phys. 117 (1995) 1.
[57] X.W. Zhou, D.K. Ward, J.E. Martin, F.B. van Swol, J.L. Cruz-Campa, D. Zubia, Phys. Rev. B 88 (2013).
[58] R.B. Vasiliev, E.P. Lazareva, D.A. Karlova, A.V. Garshev, Y.Z. Yao, T. Kuroda, A.M. Gaskov, K. Sakoda, Chem. Mater. 30 (2018) 1710.
[59] X.W. Zhou, D.K. Ward, F.P. Doty, J.A. Zimmerman, B.M. Wong, J.L. Cruz-Campa, G.N. Nielson, J.J. Chavez, D. Zubia, J.C. McClure, Prog. Photovolt. 23 (2015) 1837.
[60] X.W. Zhou, M.E. Foster, F.B. van Swol, J.E. Martin, B.M. Wong, J. Phys. Chem. C 118 (2014) 20661.
[61] X.W. Zhou, D.K. Ward, J.A. Zimmerman, J.L. Cruz-Campa, D. Zubia, J.E. Martin, F. van Swol, J. Mech. Phys. Solids 91 (2016) 265.
[62] X.W. Zhou, J.J. Chavez, S. Almeida, D. Zubia, J. Appl. Phys. 120 (2016).
[63] W. Voigt, Lehrbuch der Kristallphysik (Mit Ausschluss der Kristalloptik), B. G. Teubner, 1928.
[64] J. Nocedal, S.J. Wright, Conjugate Gradient Methods, Springer, 2006.
[65] E.J. Barbero, Finite Element Analysis of Composite Materials using AbaqusTM, Taylor & Francis, 2013.